

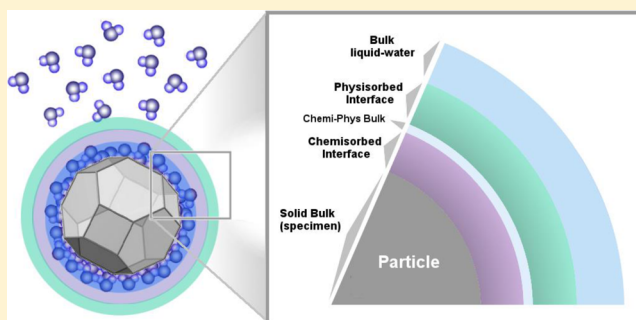
Water Adsorption Microcalorimetry Model: Deciphering Surface Energies and Water Chemical Potentials of Nanocrystalline Oxides

John W. Drazin and Ricardo H. R. Castro*

Peter A. Rock Thermochemistry Laboratory and NEAT ORU, University of California - Davis, One Shields Avenue, Davis, California 95616, United States

S Supporting Information

ABSTRACT: The surface energy of a nanomaterial is a primary characterization parameter that has important implications on the material's properties and applications including: catalysis, prediction of polymorphic stability, optimization of consolidation processes, and general colloidal science issues. However, currently, there is a dearth of techniques and theory to accurately measure surface energies for nanocrystalline solids and oxides. Therefore, we present a water adsorption microcalorimetry model using a novel second order surface energy differential equation to calculate the surface energy of anhydrous and hydrated (at any given level) nanocrystalline oxides. The experimental setup, used to feed data to the model, uses a water adsorption apparatus to measure the adsorbed water content on the specimen's surface as a function of pressure ($\sim 2 \mu\text{mol}$ dose) coupled with a microcalorimeter that can measure changes in the differential heat of water adsorption during the dosing. Using the experimental data and derived model, we can regression-fit the adsorbed water and differential heat of water adsorption data over the entire pressure range, vacuum to saturation, to calculate the surface energy via numerical integration of the second-order differential equation with the appropriate boundary conditions. We have tested the method using two technologically relevant nanoparticles, yttria doped zirconia (10YSZ) and γ -alumina. As key results, the calculated anhydrous surface energies for 10YSZ and γ -alumina are thus 1.54 ± 0.08 and $1.57 \pm 0.04 \text{ J}\cdot\text{m}^{-2}$, respectively, and correlate well with other theoretical and experimental data. The model also provides relevant information on the changes of interaction energies between water molecules and the oxide surface.



INTRODUCTION

Oxide nanoparticles exhibit remarkably different properties as compared to their bulk counterparts due to their relatively large surface area to volume ratio. This allows them to be used for advanced applications, including catalysis,^{1,2} gas sensing,^{3,4} energy storage,^{4,5} and energy conversion,^{6–8} with less material and higher efficiency. The large surface area also has been shown to alter the polymorphic stability of nanomaterials via an increase of the Gibbs free energy; some common examples include the zirconia, titania, and alumina systems.^{9–14} This happens because of intrinsic differences in the surface energies, γ , for distinct phases that can overcome crystal stability trends predicted from phase diagrams.

Accurate surface energy data is therefore of prime importance to understand phase stability, but also to understand and predict coarsening and reactivity of nanoscaled materials. Acquiring reliable thermodynamic data, in particular for ceramic oxides, is however not a trivial thing, as surface energies are very small quantities, and designing experiments to isolate this energetic contribution requires sophisticated approaches. Several methods can be found in the literature addressing this problem. Measurements of wetting angles,¹⁵ correlation of elastic modulus to the surface energy,¹⁶ crystal

cleavage work, and calorimetric approaches are among the current available techniques. Among the calorimetric ones, two main techniques have been systematically used in the past decades to determine accurate surface energies of oxides: high temperature oxide melt drop solution^{10,12,17,18} and water adsorption microcalorimetry.¹⁹ High temperature solution calorimetry requires multiple samples that have different grain sizes that are then dissolved in a calorimeter and have the enthalpy measured and related back to the surface energy using a Hess' Law engine. There is an implicit assumption that all of the samples have the same exposed crystallographic planes that produce a linear data set where the slope is the surface energy.¹⁹ This is not an overly apparent condition for many complex systems, which restricts the use of this method to simple and well behaved materials. Also, the use of a Hess's Law engine necessitates many reaction enthalpies to be used that may not exist and compound the error.

Instead, water adsorption microcalorimetry requires only a single specimen at room temperature, which is nondestructively

Received: February 14, 2014

Revised: April 21, 2014

Published: April 23, 2014

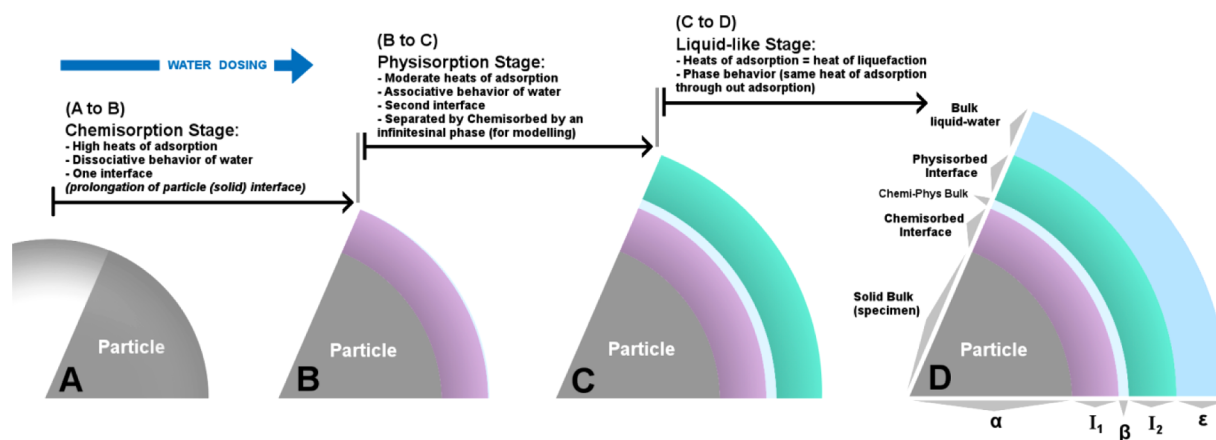


Figure 1. (A) Initially, the naked specimen's surface (gray layer) is in thermodynamic equilibrium with a vacuum. (B) The first initial dosing of water onto the sample has a dissociative character with a single interface (purple layer). The adsorption enthalpies are considerably more exothermic than liquid water. (C) The water adsorbing in the outermost layer interacts less with the surface and thus the water stays in an associative state. This adsorbing water is situated in a second interface (green layer) that is separated by an infinitesimal "bulk-like" phase (white) where the heats of adsorption diminish and approach the liquid water value. (D) Eventually, the water builds up enough monolayers so that the outermost water adsorbs with an enthalpy exactly equal to that of liquid water (light blue layer). α , β , and ϵ represent the bulk phases, while I_1 and I_2 present the interfaces between the bulk phases.

degassed to an anhydrous state and subsequently dosed with water vapor, where the quantity adsorbed is measured by a water adsorption apparatus.¹⁹ Simultaneously, a microcalorimeter is utilized to measure the energetics of the interaction of water with the powder's surface.¹⁷ Therefore, heat of adsorption data from the anhydrous (vacuum) to fully hydrated (saturation) state can be acquired and analyzed to determine the surface energy following a proposed thermochemical cycle in which the energy difference from the saturated state to the anhydrous state is simply related to the heat of adsorption and amount of adsorbed water. Because the surface energy at the saturated state is known (surface tension of liquid water), the energy state in each adsorption step can be potentially calculated. However, the approach ignores the contribution from the chemical potential of water molecules, which is the main limitation of the technique. That is, this approximation is only valid if the minimal coverage where a liquid-like state of adsorbed water is observed is used in the thermochemical cycle. Adsorption of water beyond that minimal point results in the same heat of adsorption (liquefaction of water), but no changes on the surface energy, meaning that the contribution of the water molecules chemical potential change is no longer negligible and leading to unrealistic surface energy numbers if calculation proceeds.

The minimal coverage for liquid-like state coverage is identified when the heat of adsorption becomes equivalent to water liquefaction. While the exact point at which this happens could theoretically be determined from the proposed experiment, the precise coverage is not obvious due to experimental deviations. A refined theoretical description of the adsorption process could then be used to fit the experimental data and precisely define states from the thermochemical cycle. Moreover, one could also include the contributions from water chemical potentials to the model, improving the overall reliability of the data. This is of course not an easy task, as the adsorption behavior is a complex phenomenon that has been studied for many years.

For instance, there are indications^{20–22} that during exposure of an oxide to water doses, molecules adsorb on the surface in a dissociative (chemisorption) character followed by a molecular

(physisorption) one. This change of chemistry would suggest that the adsorption process would occur via a two interface system (specimen–chemisorption and chemisorption–physisorption interfaces) rather than a single specimen–water interface. The logic behind this definition is that a chemically distinct species that preferentially forms on the first layer would act as chemical barriers to further molecules, leading to a molecular water interaction with the "coated" surface. However, there are other theories^{20,23} that suggest that both chemisorption and physisorption water form in the first monolayer, but also in the higher layers, which would complicate a two interface interpretation, suggesting a single interface model would be more appropriate.

In fact, there is no one definitive answer for the overall description of water adsorption behavior on surfaces. One of the goals of this work is therefore to explore new theoretical foundations for water adsorption using a two interface description of the specimen–water system with the hope that we shed light upon the water adsorption process. We shall compare that result with the standard, well-known equation for a single interface to determine how much the two theories differ for water adsorption and discuss experimental data that justifies the proposed two-interface model. We then use this knowledge and the derived equations to study water adsorption on oxide nanoparticles and to calculate precise surface energy values. Model materials for the study were γ -alumina and yttria stabilized zirconia nanoparticles.

THEORETICAL DESCRIPTION OF THE ADSORPTION PROCESS

Water adsorption experiments require a well characterized initial state. This is selected as the anhydrous condition to allow comparisons with theoretical calculations and to simplify replications. This state is achieved by degassing, in a vacuum tube, under moderate heat after assuring from a thermogravimetric study that that degassing condition is adequate to fully remove all adsorbed water. The adsorption study starts by dosing the system with small amounts (e.g., $\sim 2 \mu\text{mol}$) of water vapor and measuring the pressure after establishing thermodynamic equilibrium. Physically, the vapor gradually adsorbs onto

the powder's surface, leading to the creation of a transitional layer of water that gets thicker with increasing doses. At low coverage, it has been suggested that the system can be treated as a single interface, with the water vapor attached to the specimen's surface and subsequently, expanding from the surface. This indicates that the Gibbs adsorption isotherm can be used to connect the surface energy to adsorbed water quantity as proposed previously.²⁴ However, for high coverage, when a thick water layer exists, it has been proposed that a solid–liquid interface is formed between the specimen and the adsorbed water, followed by a liquid–vapor interface. At this configuration, an extension of the Gibbs adsorption isotherm can be applied, but the determination of absolute surface energies directly for water adsorption amounts alone becomes impractical as the thermodynamics of the solid–liquid interface plays a major role.^{24,25}

From the molecular point of view, it has been suggested^{20–22} that the adsorbed water interacts with the surface in two different ways: dissociative (chemisorption) and molecular (physisorption). Castro and Quach¹⁹ attempted to combine this view with the macroscopic perspective described above, postulating that the solid–liquid interface is formed when and after water molecules showed associative behavior. This concept was not further developed in their work but opened a question regarding the precise definition of a bulk or an interface in this problem and, hence, on the usage of Gibbs adsorption isotherm concepts.

In this work we propose a more detailed description of the adsorption process using a more strict definition of interfaces. That is, interfaces are transient in nature and are defined by the gradients of the components' concentrations such that they have a finite thickness that separates bulk phases and depends on the quantity of water adsorbed. To understand this idea, let us assume a naked surface, as shown in Figure 1. The particle (specimen) is defined as a bulk phase. As water adsorbs onto its surface, molecules suffer dissociation, but not all reactions show similar enthalpies,¹⁹ revealing that the water molecules that reacted first are in a different thermodynamic state as compared to those reacting later on in the adsorption process. So, one may define the chemisorbed zone (transient state from A to B, see Figure 1) as an interface itself. Eventually, as adsorption proceeds, chemisorption energy becomes constant, and therefore, a negligible, physisorption process begins where molecules only interact associatively with the surface. At this point, the molecules are also in a transient state (from B to C), as their states change with the distance from the chemisorbed interface (heats of adsorption are not constant¹⁹). So, one may also define the physisorbed zone as an interface as well. As two interfaces must be separated by a finite bulk region, one may theoretically introduce an arbitrary bulk phase separating them (though not precisely defined in terms of location or thermodynamic variables, but with a negligible thickness). As adsorption proceeds (from C to D), the water achieves a liquid-like state. From this point on, the distance of the adsorbed molecule from the surface does not affect its properties, and therefore, this region can be called a bulk phase. A sharp liquid–vapor interface then exists with a constant surface energy with the adsorption of additional water.

Based on this description of the process, a Gibbs adsorption isotherm that incorporates two interfaces is needed to fully describe the water adsorption process (assuming no contribution from the zero-thickness liquid–gas interface). An equation

that governs this process can be derived from the general Gibbs free energy, eq 1.

$$G = U + PV - TS + \sum_i \theta_i \mu_i \quad (1)$$

$$G_T = G^\alpha + G^\beta + G^\varepsilon + G^{I_1} + G^{I_2} + \gamma SA \quad (2)$$

For a three phase system with two interfaces, eq 2 represents the linear combination of the different species, where the surface excess term is factored out to determine the total Gibbs free energy of the system where α , β , and ε are the bulk phases for the specimen (particle), the chemisorption–physisorption bulk phase, and liquid–water-like phase, respectively, and I_1 and I_2 are for the chemisorption and physisorption interfaces, respectively. The surface energy, γ , is measured from the outermost layer of adsorbed water in equilibrium with the water vapor or vacuum; refer to Figure 1. From the above definitions, one can derive the Gibbs adsorption isotherm for two interfaces, with a detailed derivation found in Appendix.

$$SA \times d\gamma = - \sum_{I_1, I_2} \left(\sum_i \theta_i d\mu_i \right) \quad (3)$$

In this new adsorption equation, the summation over i corresponds to the excess constituents in a given interface where μ is the chemical potential, θ is the adsorbed amount in moles, γ is the surface energy, and SA is the surface area measured using BET theory.²⁶ Note this equation looks very similar to the single interface Gibbs adsorption isotherm, eq 4, where there is only one summation for the single interface:

$$SA \times d\gamma = - \sum_i \theta_i d\mu_i \quad (4)$$

From eq 3, we can define a new variable, μ_{ads} , which is the average chemical potential of all adsorbed constituents in both of the interfaces (averaging all chemisorbed and physisorbed water).

$$\mu_{\text{ads}} \equiv \frac{\sum_{I_1, I_2} (\sum_i \theta_i \mu_i)}{\sum_{I_1, I_2} (\sum_i \theta_i)} \quad (5)$$

$$\theta = \sum_{\beta, I_1, I_2} \left(\sum_i \theta_i \right) \quad (6)$$

Note that the denominator in eq 5 is equal to the total amount of water molecules adsorbed in the chemisorption and physisorption interface regions alone. The total amount of water adsorbed during the experiments (counting bulk and interfacial zones) is thus given in eq 6 where the third summation accounts for the water in a chemisorption–physisorption separation phase as well.

The thickness of this separation zone is not well-known, but some works suggest it to be on the molecular scale, being a few monolayers or so^{20–23} at most. The transition to the physisorption state is however not expected to be abrupt as suggested in Figure 1, and water states are expected to (or at least can) be intermixed in many of the adsorbed layers. Therefore, one may assume the thickness of the bulk phase β separating physisorbed and chemisorbed behaviors to be negligible, simplifying coverage and chemical potential descriptions to eqs 7 and 8. Note that the bulk phase β was previously and artificially introduced in the model for the adsorption process in order to separate chemi- and physisorbed zones. The fact they are possibly intermixed suggests the

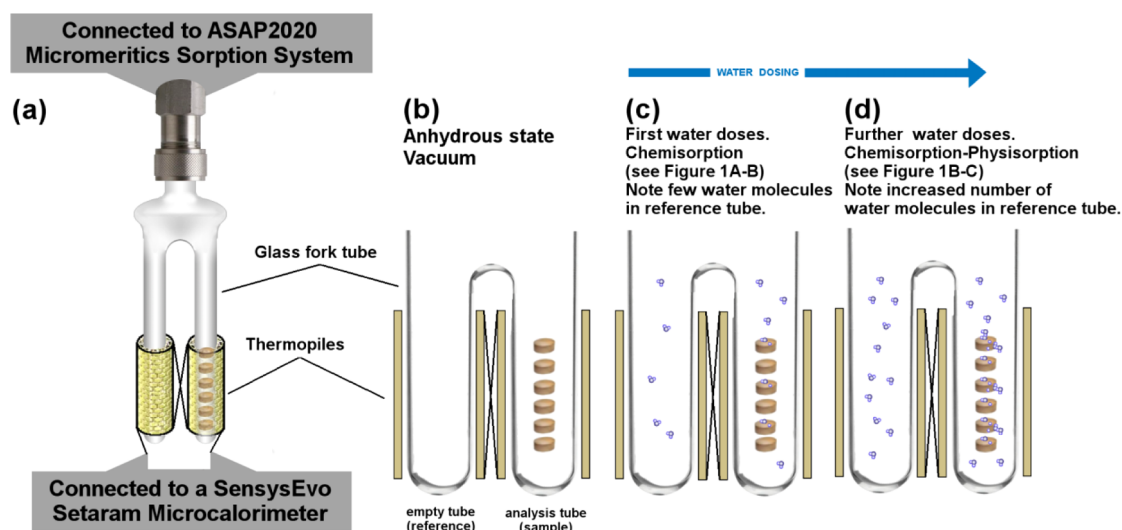


Figure 2. (a) The schematic diagram of the experimental setup is shown. The fork tube is situated inside of a Setaram SensysEvo microcalorimeter with the specimen in the right fork where thermopiles surround both forks to measure the enthalpies of adsorption. The fork tube is then connected to an ASAP 2020 sorption system to introduce the water vapor to the specimen and system. (b) The initial state of the experiment where the specimen is degassed and there are no water molecules in the system. (c) The ASAP 2020 introduces a small dose of water ($\sim 2 \mu\text{mol}$). The system re-establishes equilibrium by adsorbing water on the sample. Note the pressure in the reference and sample forks will be equal at the new equilibrium. ASAP 2020 measures the pressure and water coverage after the system reaches equilibrium. The thermopiles measure simultaneously the energetics of the adsorption step and report the difference between the right (sample) and left (reference) forks. (d) Another dose of water from the ASAP 2020 machine is introduced into the system. Water vapor again adsorbs onto the specimen to re-establish equilibrium. The dosing repeats until the desired relative pressure is reached.

nonexistence of this bulk phase, though it is necessary for a rigorous thermodynamic description. An average of the chemical potentials from both chemisorption and physisorption zones is used in eq 5, though acknowledging the absence of a sharp transition and without compromising the thermodynamic formality.

$$\theta \approx \sum_{I_1, I_2} \left(\sum_i \theta_i \right) \quad (7)$$

$$SA \times d\gamma = -\theta d\mu_{\text{ads}} + d\mu_{\text{ads}} \sum_{\beta} \left(\sum_i \theta_i \right) \approx -\theta d\mu_{\text{ads}} \quad (8)$$

Therefore, we can use eqs 5 and 7 and insert them into the appendix derivation utilizing the physical constraint that the Gibbs–Duhem equation applies equally to the individual species as well as the macroscopic visualization of the system to rewrite the adsorption isotherm.

Note that, with this definition, we have simplified the physics of the adsorption process because we no longer keep track of the constituents in the interfaces as well as how much water is in each chemical state. Instead, we have written the equation using the total water quantity adsorbed from the experimental measurements as a variable, which simplifies the equation and reduces the number of variables. Unfortunately, there is no available theoretical framework to deconvolute the adsorbed chemical potential from a single isotherm measurement. Therefore, in order to use eq 8 to determine surface energies, we need to develop another equation that explicitly incorporates the adsorbed chemical potential. This is derived below based on the energetics of the adsorption reaction.

Heat of adsorption can be assessed using a combined sorption system and a microcalorimeter. We used this system to describe the adsorption phenomenon and equate the chemical potential dependences, so limitations may apply for other adsorption setups. The microcalorimeter used here was a

differential scanning calorimeter operated at room temperature and that has two ports to accept a glass fork tube, as detailed elsewhere.^{17,19} Refer to Figure 2a for a schematic drawing of the reaction chamber. Initially, the system in Figure 2b is at the initial reference state where a dehydrated specimen of negligible volume is located in the right fork tube under a vacuum. Next, a dose of water vapor is injected into the fork tube and some of the vapor adsorbs onto the surface of the specimen, while the remaining vapor is distributed among the two forks to establish equilibrium, Figure 2c. Again, another dose of vapor is injected so that more water is adsorbed onto the surface and the remaining vapor is redistributed to establish equilibrium once more, Figure 2d. This process is repeated ideally at differential doses from vacuum to the saturation pressure.

Initially the system is in chemical equilibrium, so one can write out the Gibbs free energy for both forks similar to eq 1 using the adsorbed chemical potential definition. Also the Gibbs free energy can be reduced by utilizing the first law of thermodynamics for each fork; as in eqs 9 and 10, where H is the enthalpy, S is the entropy, μ_{ads} is the adsorbed chemical potential, μ_{gas} is the vapor chemical potential, θ is the adsorbed water, N is the vapor in each fork, and γSA is the surface excess.

$$G_{\text{R}} = H_{\text{R}} - TS_{\text{R}} = \theta \mu_{\text{ads}} + N_{\text{R}} \mu_{\text{gas}} + \gamma SA \quad (9)$$

$$G_{\text{L}} = H_{\text{L}} - TS_{\text{L}} = N_{\text{L}} \mu_{\text{gas}} \quad (10)$$

Note the Gibbs free energy is written separately for the two sides of the fork tube (left, G_{L} , and right, G_{R}) because the experiments will provide the enthalpy difference between the two (DSC setup). Therefore, one can determine a reaction Gibbs free energy change by allowing a differential vapor dose in each fork, dN , and letting $d\theta$ water molecules adsorb on the specimen's surface to re-establish equilibrium. Therefore, one can subtract the initial and final Gibbs free energies in both sides of the tube to develop a differential change.

$$dG_R = d\theta\mu_{\text{ads}} + (dN - d\theta)\mu_{\text{gas}} + d(\gamma SA) \quad (11)$$

$$dG_L = dN\mu_{\text{gas}} \quad (12)$$

As the measured heat will be the differential from both tubes, the subtraction of eqs 11 and 12 will determine the free energy change during each dosing “reaction”, assuming the volume of the powder is negligible.

$$dG_{\text{reaction}} = d\theta(\mu_{\text{ads}} - \mu_{\text{gas}}) + d(\gamma SA) \quad (13)$$

$$dH_r = TdS_r + (\mu_{\text{ads}} - \mu_{\text{gas}})d\theta + d(\gamma SA) \quad (14)$$

One can see that there is a difference in chemical potentials in eq 14 which may elicit concern because at equilibrium the chemical potential of the surface species should be equal to the vapor chemical potential. However, it is important to remember the defined adsorbed chemical potential is an average over all constituents (dissociated and molecular water) in all of the interfaces, so there is no explicit reason to assume that it will always be equal to that of the vapor potential. This logic exists because there is no physical constraint on the dissociated water to be at the vapor chemical potential at equilibrium as it is a different chemical species than molecular water.

The next step is to determine the entropy change of the overall dosing reaction, dS_r , which is simply the entropy of condensation in the right fork since the other entropic terms associated with the dosing are canceled from the measurements due to the design of the experiment. One can visualize this concept logically breaking up the process into a two-step path, where first both forks come into equilibrium with the water dose without adsorption and then allowing adsorption in the second step.

Next, we need to deconvolute the average chemical potential into a function of the adsorbed quantity and an additive constant, as shown in eq 15. There the chosen constant is the summation of the specific enthalpy of condensation and specific entropy of condensation evaluated at the saturation pressure, p_o . This constant is chosen because at the saturation pressure (high coverage) the chemical potential should be close to the bulk water chemical state.

$$\mu_{\text{ads}}(\theta) \equiv F_{\mu}(\theta) + \left. \frac{dH_{\text{con}}}{d\theta} \right|_{T_o, p_o} - T_o \left. \frac{dS_{\text{con}}}{d\theta} \right|_{T_o, p_o} \quad (15)$$

$$\frac{d\mu_{\text{ads}}}{d\theta} = \frac{dF_{\mu}(\theta)}{d\theta} \quad (16)$$

Note that $F_{\mu}(\theta)$ is just a reference function created with units of chemical potential to isolate the additive constants. It is imperative to note that the derivatives of the adsorbed chemical potential and $F_{\mu}(\theta)$ are equivalent and either one can be used in the derived Gibbs adsorption isotherm equation. Plugging eq 15 into eq 14 yields the final differential heat of adsorption equation where we assume that the entropy of condensation does not strongly depend on the pressure so that the two entropy terms cancel.

$$\frac{dH_r}{d\theta} = F_{\mu}(\theta) - \mu_{\text{gas}} + \left. \frac{dH_{\text{con}}}{d\theta} \right|_{T_o, p_o} + \frac{d(\gamma SA)}{d\theta} \quad (17)$$

Note eq 17 represents the differential heat of adsorption enthalpy that is actually measured using the microcalorimetric setup from Figure 2. This equation relates the measured data to

differences in the chemical potentials, changes in the surface excess, and the enthalpy of water condensation at the saturation pressure, which is $-44 \text{ kJ}\cdot\text{mol}^{-1}$ at 25°C .

Now we have derived two equations, 8 and 17, that relate the adsorbed chemical potential to the surface energy for a given water adsorption process. Therefore, a single differential equation for the surface energy can be solved by inserting eq 8 into the derivative of eq 17.

$$\frac{d^2 H_r}{d\theta^2} + \frac{d\mu_{\text{gas}}}{d\theta} = \gamma \frac{d^2 SA}{d\theta^2} + \left(2 \frac{dSA}{d\theta} - \frac{SA}{\theta} \right) \frac{d\gamma}{d\theta} + SA \frac{d^2 \gamma}{d\theta^2} \quad (18)$$

Equation 18 is a general second-order surface energy differential equation which does not depend on the adsorbed chemical potential and instead relies on $d^2 H_r/d\theta^2$, $d\mu_{\text{gas}}/d\theta$, and SA , which are all known or measurable quantities. This equation is powerful because it bypasses any assumption on the functional form of the adsorbed chemical potential (chemical state of the water), which is prevalent in the literature,^{24,27–31} and all that is needed to solve this differential equation is to specify the boundary conditions.

As the pressure reaches saturation, we expect the adsorbed water to approach infinity and the surface energy to approach the bulk liquid water value which at 25°C is $0.072 \text{ J}\cdot\text{m}^{-2}$. Finally, the derivative of the surface energy should converge to zero at the saturation pressure because the surface energy approaches a constant. With these boundary conditions, a unique answer will be determined for every measured specimen. However, it becomes difficult to numerically integrate equations with a domain from zero to infinity, so eq 18 will be transformed into eq 19 by forcing the surface energy to be a function of the pressure instead.

$$SA \frac{d^2 \gamma}{dx^2} = \frac{d\theta}{dx} \left\{ \frac{d^2 H_r}{d\theta^2} \frac{d\theta}{dx} + \frac{d\mu_{\text{gas}}}{dx} - \gamma \frac{d^2 SA}{d\theta^2} \frac{d\theta}{dx} + \frac{d\gamma}{dx} \left(\frac{SA}{\theta} - 2 \frac{dSA}{d\theta} + SA \frac{d^2 \theta}{dx^2} \left(\frac{dx}{d\theta} \right)^2 \right) \right\} \quad (19)$$

Equation 19 is theoretically equivalent to eq 18 but is mathematically preferred because the step size of the relative pressure can be kept constant throughout the integration, which is not easily done with the adsorbed water domain. Note that, in eq 19, it was implicitly assumed that x is the relative pressure (p/p_o), the adsorbed water is a function of the pressure, and the differential heat of water adsorption is a function of the adsorbed water, θ . Note that the boundary condition for the surface energy remains unchanged, but the relative pressure derivative of the surface energy approaches a negative constant instead.

In order to numerically integrate the above differential equation, the measured data must first be fitted to regression equations because derivatives of the data are required and continuous functions will provide more reliable surface energies. Therefore, regression equations over the entire pressure domain are needed for the adsorbed quantity and the differential heat of water adsorption. First, we will look at the adsorbed quantity which has the functional form similar to other measured water isotherms.^{24,26–28,32–34} Unfortunately, none of the theories or empirical equations completely describes the adsorption isotherm without using a power law series. Instead, we will attempt to provide a simple model that

fits the adsorption model over the entire pressure range. Since the adsorption reaction is a kinetic-based process, one can expect that the chemisorption first layer will be built up at locations where there is no adsorbed water while at other locations there could be physisorption proceeding simultaneously. With this assumption, one can write a water adsorption isotherm equation as

$$\theta = \theta_{\text{chemi}} + \theta_{\text{physi}} \quad (20)$$

ignoring any higher order interaction or mixing terms. This simplifies the problem to finding the most appropriate model that fits chemisorption and physisorption theory. With this in mind, the most popular physisorption model is BET theory.²⁶ For chemisorption, there are suggestions^{20–23} that the majority of the first layer of water disassociates on the surface of the specimen suggesting that we should use the dissociative Langmuir adsorption isotherm to model it. Combining these two models, we can rewrite eq 20 as

$$\theta = \theta_c \frac{b\sqrt{x}}{1 + b\sqrt{x}} + \theta_p \frac{cx}{(1-x)(1+(c-1)x)} \quad (21)$$

Equation 21 is the regression equation used to fit the water adsorption data as a function of pressure and relies only on four variables: θ_c , which is the monolayer coverage of the dissociative water on the first layer, θ_p , which is the physisorption monolayer coverage from BET theory, and b and c are unitless fit parameters that depend on the specimen.

Next we have to determine a functional form for the differential heat of water adsorption data. However, there currently is no theory to deal with the differential heats of water adsorption that are measured, so any regression equation will be purely empirical. After looking at many differential heats of water adsorption curves from the literature and measured in our laboratory, it seems that a simple exponential expression can be used with a high degree of accuracy for most materials.

$$\frac{dH_R}{d\theta} = D e^{-\theta/d} + E(f\theta - \theta^2) e^{-\theta/e} + \left. \frac{dH_{\text{con}}}{d\theta} \right|_{T_{\text{on}}, p_0} \quad (22)$$

Equation 22 is then an empirical relationship for the differential heat of water adsorption as a function of the water coverage, which requires five experimental parameters where d and e are decay parameters that relate how strong the specimen's surface affects the adsorbed water, and D , E , and f are just fit parameters with units of $\text{kJ}\cdot\text{mol}^{-1}$, $\text{kJ}\cdot\text{mol}^{-3}$, and mol , respectively.

The surface area of the specimen should not change appreciably throughout the dosing, but a regression equation is still required because at the saturation pressure an infinite surface area is expected. Therefore, we will assume a simple linear form with the water quantity as the independent variable. The change in the surface area with coverage will be determined from an approximation that all the surface area can adsorb an infinite number of water layers²⁶ so that we can rearrange the surface area to create a larger sphere where the first order linear correction to the surface area will be used as the linear constant.

$$\text{SA} = \text{BET} + A\theta \quad (23)$$

■ EXPERIMENTAL METHODS

Synthesis and Characterization of γ -Alumina and 10YSZ. γ -Alumina was synthesized via a polymeric precursor

method^{35,36} by mixing aluminum nitrate (25 wt %) in citric acid (45 wt %) and ethylene glycol (30 wt %) to form a clear, dilute solution. This mixture was heated to 120 °C to activate polyesterification and the formation of the metal chelates. The remaining resin was heat treated at 650 °C for 4 h to form a powder consisting of aluminum hydroxide and residual carbon material. This powder was then heated to 800 °C for 12 h under air flow to burn off the residual carbon and to decompose the hydroxide to nanocrystalline γ -alumina. A Bruker Equinox 55 FTIR spectrometer for mid- and near-IR range analysis was utilized to detect the presence of any remaining organic residuals and carbonate phases via infrared spectroscopy.

10YSZ (10 mol % Y_2O_3 doped ZrO_2) was synthesized via a modified reverse strike coprecipitation method^{35–37} by mixing the yttrium nitrate hexahydrate (3.8301 g) and zirconium nitrate hydrate (12.144 g) in water (0.15 L) to form a clear, dilute solution. This mixture was dropped point-wise into a stirred 1 M excess ammonium hydroxide solution (0.25 L). The resultant mixture was washed three times using as solvents for the first wash 100% water, second wash 50% water and 50% ethanol, and finally 100% ethanol. The powder was subsequently dried overnight at 90 °C. The dried hydroxide powder was heat-treated at 450 °C for 2 h to burn off any ethanol residue and to produce the nanocrystalline cubic fluorite 10YSZ.

Thermogravimetry showed significant mass loss due to water adsorption up to 750 and 450 °C for γ -alumina and 10YSZ, respectively. Therefore, these temperatures were used for degassing prior to both BET and water adsorption experiments. X-ray diffraction using a Bruker-AXS D8 Advance diffractometer (Bruker-AXS, Inc.) was used to study the samples which was operated with a 40 kV accelerating voltage with a 40 mA emission current utilizing a copper X-ray source target.

Adsorption Microcalorimetry. The water adsorption microcalorimetric experiments require an ASAP 2020 Micromeritics, equipped with turbo pumps and a furnace for degassing at elevated temperatures, coupled with a Calvet-type microcalorimeter (Setaram DSC-111) to perform the experiments. The ASAP 2020 measures the serial relative pressures and adsorbed water quantities while the microcalorimeter measures the heat evolved during the adsorption process (that combined with the adsorption data gives enthalpies of adsorption).¹⁷ Figure 2a shows a schematic diagram of this setup. The sample is placed in the right leg of the fork tube (analysis chamber), while the left leg is used as a reference where the microcalorimeter records the heat flow difference between the forks as in a normal DSC experiment. The thermochemical cycle for the experiments is described below in eq 24, where $n_{\text{H}_2\text{O}}$ is the number of moles of water vapor adsorbed in each dose and $dG/dn_{\text{H}_2\text{O}}$ is the Gibbs free energy of the water in $\text{kJ}\cdot\text{mol}^{-1}$. The cycle looks at the energetics of the initial state, where the surface is pristine with no adsorbed water, but with water vapor in the system, as compared to the final state, where the surface energetics are modified due to the adsorption of the water vapor. Note that the energy released in the cycle depends on the lowering of the surface energetics and the lowering of the vapor's Gibbs free energy by adsorption. This cycle holds true if and only if there are no other irreversible reactions proceeding throughout the adsorption process which is assumed in the aforementioned derivations.

$$\begin{aligned}
 &SA \times \gamma(\text{surface}) + n_{\text{H}_2\text{O}} \times \frac{dG_{\text{gas}}}{dn_{\text{H}_2\text{O}}} \\
 &\rightarrow SA \times \gamma'(\text{surface}') + n_{\text{H}_2\text{O}} \times \frac{dG_{\text{ads}}}{dn_{\text{H}_2\text{O}}} \quad (24)
 \end{aligned}$$

The microcalorimetric experiments require a large specimen surface area compared to the fork tube's area. Thus, a total surface area of 2–5 m² was used for both experiments, which corresponds to 10–20 mg of degassed powder but really depends on the individual sample (as each has a different specific surface area). The samples were degassed at 750 °C for 12 h and 450 °C for 12 h for γ -alumina and 10YSZ, respectively. After degassing, the sample chamber was maintained by the microcalorimeter at 25 °C with a dosing of $\sim 2 \mu\text{mol}$ of water, which was maintained and monitored by the ASAP 2020. The initial equilibrium delay was ~ 1.5 h, which was reduced to half an hour at the higher relative pressures (the equilibrium time was designed to be enough for the measured heat signal in the calorimeter to return to the baseline, this time shortens at higher coverages). Three sets of experiments were performed: one for γ -alumina, 10YSZ run 1 (2.25 m²), and 10YSZ run 2 (4.69 m²). A blank run (empty tube) was made to remove any water that adsorbed onto the walls of the fork tube and manifold instead of the specimen. The microcalorimeter was calibrated against the enthalpy of fusion for gallium.

Numerical Integration. The experimental data was computed using a custom written MATLAB 2010a function where the data was fit to eqs 21 and 22 so that the surface energy differential equation could be numerically integrated using a relative pressure step size of 5×10^{-10} with units of p/p_0 starting near the saturation pressure with the aforementioned boundary conditions. The initial relative pressure was $1 - 5.8 \times 10^{-17}$ because this is the closest value to 1 in the 32-bit programming that is different from unity. The surface energy pressure derivative was solved with step size of 1×10^{-5} , with starting surface energy on the order of $50 \text{ J} \cdot \text{m}^{-2}$, to converge the result in a timely manner. The anhydrous surface energy was selected at the ideal vacuum reference state, where relative pressure is identical to zero.

RESULTS AND DISCUSSION

Figure 3 shows the X-ray diffraction patterns for γ -alumina and 10YSZ. The two patterns were indexed according to the expected crystallographic structures and confirm the presence of the gamma spinel structure for the alumina powder and the cubic fluorite structure for the 10YSZ powder. Also, the patterns showed a lack of impurities in both. Infrared spectroscopy and thermogravimetry experiments confirmed the lack of organic compounds and carbonate phases for the γ -alumina powder, which was synthesized via a polymeric precursor method. Cryogenic N₂ gas adsorption (BET method) showed that the powders had a surface area of 186.7 ± 3.8 and $154.6 \pm 0.7 \text{ m}^2 \cdot \text{g}^{-1}$ for γ -alumina and 10YSZ, respectively, which is sufficiently high for accurate microcalorimetric studies.

Figures 4 and 5 show the adsorption isotherms, water coverage as a function of relative pressure, and the differential heats of adsorption as a function of relative pressure or water coverage for the γ -alumina and 10YSZ experiments, respectively. The adsorption isotherms have the same relative shape to one another as well as in previous experiments in the literature,^{17,38–41} which have a few distinct regions that are differentiated by the isotherm's derivative. The first region

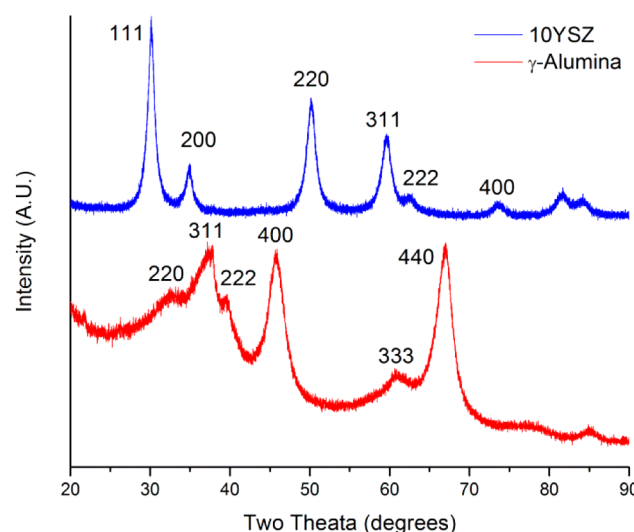


Figure 3. X-ray diffraction patterns for nanocrystalline γ -alumina (red, bottom) prepared via a polymeric precursor method and 10YSZ (blue, top) prepared via a reverse strike coprecipitation method.

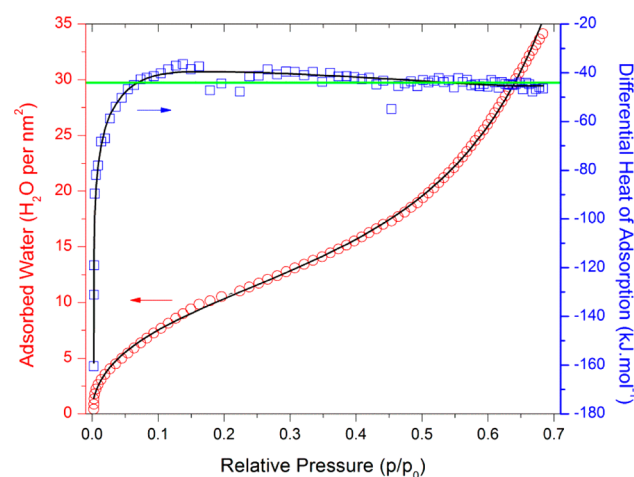


Figure 4. Water adsorption isotherm (red circle, left) of γ -alumina which was corrected with an empty tube experiment using the same conditions. Differential heats of adsorption (blue square, right) as a function of relative pressure of the water adsorbed on the γ -alumina nanoparticles. The data converges to the enthalpy of water condensation (green line) at the higher pressures. The black lines show the regression fits of the data using eqs 21 and 22. The data and regression fits coincide well.

occurs at small relative pressures (<0.02) where there is a large, linear, and sharp increase in the adsorbed water with an increase of pressure, which is due to the high reactivity of the anhydrous surface. This region is followed by an isotherm with decreasing slope up to a relative pressure of ~ 0.3 after which the slope changes (concavity as well) and begins to increase quickly at the higher pressures in the new region. The regression fit parameters for the adsorption isotherm are shown in Table 1, which uses eq 21 using the MATLAB 2010a curve fitting toolbox. The regression functions fit the data well with adjusted R -square values that exceed 99.9% over the entire experimentally collected relative pressure, which ranges from 0 to 0.7 (the reliability limit of the used adsorption apparatus under the designed experimental conditions).

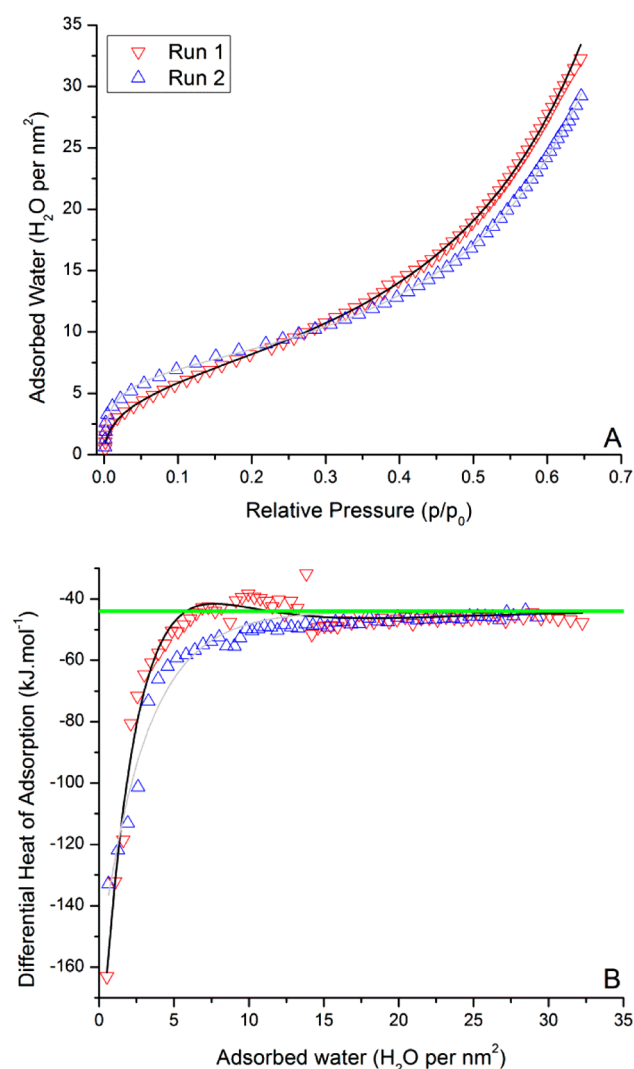


Figure 5. (A) Water adsorption isotherms for 10YSZ run 1 (red triangle) and run 2 (blue triangle) which were corrected with an empty tube experiment using the same conditions. (B) Differential heats of adsorption as a function of water coverage on the 10YSZ nanoparticles during run 1 (red triangle) and run 2 (blue triangle). The data converges to the enthalpy of water condensation (green line) at the higher pressures. The black and gray lines show the regression fits of the data using eqs 21 and 22 for runs 1 and 2, respectively. The data and regression fits coincide well.

The measured adsorption enthalpies are more negative than the condensation enthalpy of bulk water at the initial dosing, but decrease in modulus to the bulk value at higher coverages in what seems to follow an exponential function (supporting the usage of eq 22; $R^2 > 95\%$). This high initial adsorption enthalpy at lower coverages is indicative of dissociative water as

described elsewhere.⁴² The enthalpies of adsorption diminish with increasing coverage and tend toward the bulk water condensation enthalpy of $-44 \text{ kJ}\cdot\text{mol}^{-1}$. However, some of the differential heats of adsorption actually eclipse the bulk value (γ -alumina and 10YSZ run 1), while others (10YSZ run 2) always stay below this value (Table 2). It has been suggested by Bolis et al.⁴³ that this can be accounted for by some hydrophobic sites on the nanoparticles, which would justify the presence of heats of adsorption below (in modulus) $-44 \text{ kJ}\cdot\text{mol}^{-1}$. However, we present here two 10YSZ runs that were performed with the same powder and conditions, except for the surface area of the sample used in each experiment. Because of the surface area of the samples, the effective water dose density in run 2 is roughly half compared to run 1. This suggests that the “overshoot” observed in run 1 can be attributed to kinetic limitations of the water adsorbing on the surface. That is, the less water per nm² in each dose allows the system to reach a global thermodynamic equilibrium at each dose (molecules find the most stable adsorbing site). The higher doses may not allow this accommodation, leading to disordered adsorption profiles (stabilized by entropic term) that allow lower heats of adsorption as compared to the bulk water. However, all the measured enthalpies are still negative, which allows the water to adsorb spontaneously at the given temperatures. Moreover, for run 1, the adsorbed water molecules are expected to accommodate at more stable sites as the dosing progresses, such that the final states are the same (as the calculations will show).

Figures 6A,B and 7A show the surface energy curves as a function of relative pressure and water coverage calculated using our model (using the fitted data and solving the differential equation). The anhydrous surface energies for γ -alumina and 10YSZ are determined to be 1.57 ± 0.04 and $1.54 \pm 0.08 \text{ J}\cdot\text{m}^{-2}$, respectively. The 10YSZ data was averaged over the two experiments that were 1.50 ± 0.08 and $1.58 \pm 0.08 \text{ J}\cdot\text{m}^{-2}$ for runs 1 and 2, respectively, which are statistically the same value due to the overlapping error bars. The errors associated with this technique are calculated from the average of the absolute differences between the differential heats of adsorption and the regression curve where it is assumed the true values came from the regression fit. The water coverage data was not included because the regression curve fits so well that the final error would not change appreciably. The relative errors associated with this model are thus on the order of 2–10%, depending on the differential heats of adsorption, which can be difficult to obtain due to the nature of the data.

The anhydrous surface energies in this work compare well to other literature data as shown in Table 3. The experimental results the literature report 1.54^{19} and $1.53^{10} \text{ J}\cdot\text{m}^{-2}$ for γ -alumina and $1.51^{44} \text{ J}\cdot\text{m}^{-2}$ for 10YSZ. Though the results from theoretical calculations are harder to compare because each plane has its own surface energy and the water adsorption

Table 1. Regression Fit Parameters Used to Fit the Adsorption Data Using Eq 21^a

	$\theta_{\text{chemi}} (\mu\text{mol})$	b	$\theta_{\text{physi}} (\mu\text{mol})$	c	$R^2(\text{adj.})$	BET (m^2)	$A (\text{m}^2\cdot\text{kmol}^{-1})$
γ -alumina	142.70	0.8804	146.07	0.1224	0.9994	2.6650	0.180 37
10YSZ run 1	49.804	1.8920	111.27	0.2376	0.9998	2.2480	0.196 39
10YSZ run 2	71.437	6.8022	231.71	0.1901	0.9995	4.6877	0.136 00

^aThe adjusted R^2 is shown to represent how well the regression function and parameters chosen fit with the collected adsorption data. The BET column is the measured surface area of the powder used in the individual experiments from BET theory. The last column, A , is the first order approximation to the surface area increase due to adsorbing more water on the particle's surface.

Table 2. Regression Fit Parameters Used to Fit the Differential Heats of Adsorption Using Eq 22^a

	D (kJ·mol ⁻¹)	d (μmol)	E (TJ·mol ⁻³)	e (μmol)	f (μmol)	R^2 (adj.)
γ-alumina	-143.02	9.0300	7.6260	39.196	94.4744	0.9898
10YSZ run 1	-154.27	22.727	9.4850	13.237	1,509.1	0.9681
10YSZ run 2	-113.96	23.539	N/A	N/A	N/A	0.9592

^aThe adjusted R^2 is shown to represent how well the regression function and parameters chosen fit with the collected differential enthalpy data. Note that the 10YSZ run 2 does not incorporate all of the parameters in comparison to run 1.

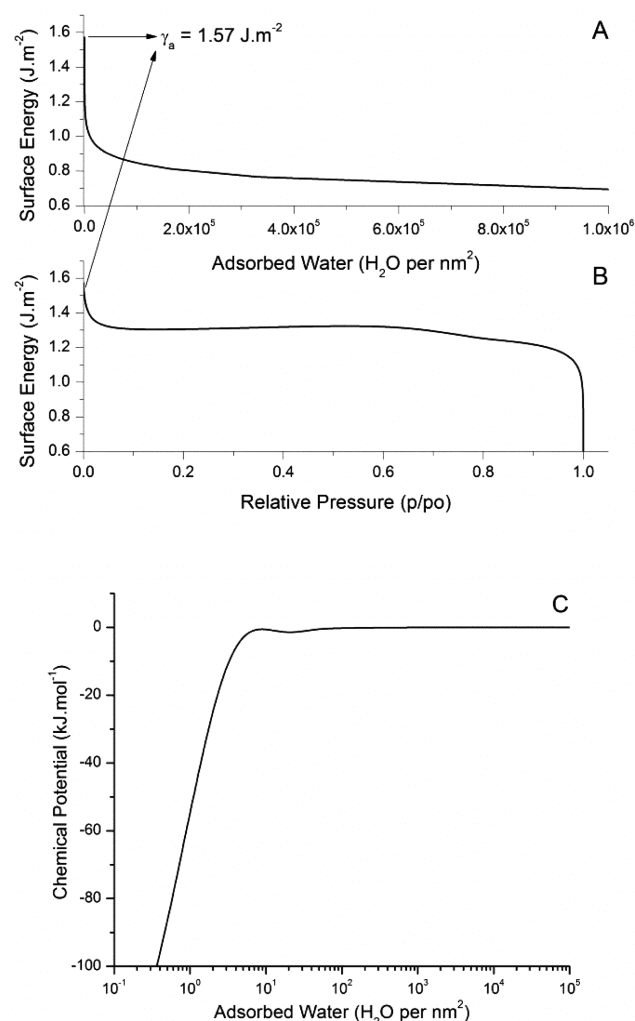


Figure 6. (A) Surface energy of γ -alumina as a function of water coverage. The anhydrous surface energy of the γ -alumina is 1.57 J·m^{-2} and then decays to the bulk water surface energy at large water coverages (not shown). (B) Surface energy of γ -alumina as a function of relative pressure. The surface energy decays from the anhydrous value, but plateaus at relative pressures between 0.1 to 0.6 before the surface energy sharply decays to the bulk water surface energy as the relative pressure approaches unity. (C) Chemical potential of the adsorbed water as a function of the water coverage. The data decays very rapidly with coverage and eventually approaches zero, as expected when the bulk liquid water is in chemical equilibrium with its vapor phase.

experiments calculate an average surface energy over all exposed planes; still the results from our experiments lie within the average of the data collected from the literature for these samples. Of course, a detailed surface characterization of the samples studied here is required to compare our results with theoretical DFT calculations, but this is beyond the scope of this work.

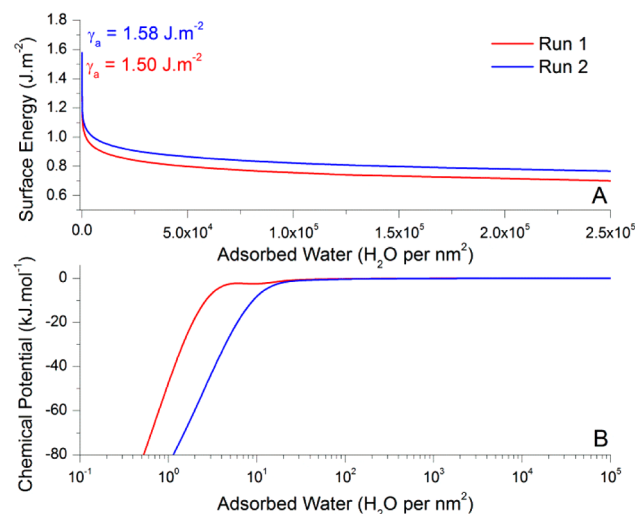


Figure 7. (A) Surface energy of 10YSZ as a function of coverage for run 1 (red) and run 2 (blue). The anhydrous surface energy for runs 1 and 2 are 1.50 and 1.58 J·m^{-2} , respectively. With an error of 0.08 J·m^{-2} for each experiment and, thus, are statistically the same point for an average of 1.54 J·m^{-2} . The anhydrous surface energy decays to the bulk water value at large water coverages (not shown). (B) Chemical potential of the adsorbed water as a function of the water coverage. The data decays very rapidly with coverage and eventually approaches zero as expected when the bulk liquid water is in chemical equilibrium with its vapor phase.

Table 3. Anhydrous Surface Energies in J·m^{-2} Calculated from the Water Adsorption Experiments, which are Compared to Other Experiments (Water Adsorption and Drop Solution Calorimetry) and Theoretical Calculations, as Cited^a

	this work	literature
$\gamma\text{-Al}_2\text{O}_3$	1.57	1.54^{19} 1.53^{10} $0.97^{(100)}$; $1.54^{(110)}$; $1.97^{(111)45}$ $1.05^{(100)}$; $1.53^{(110)}$; $1.85^{(111)48}$
10YSZ	1.54	1.51^{44} $\sim 1.05^{(111)}$; $\sim 1.95^{(110)49}$

^aSuperscripts in parentheses denote crystallographic surface planes.

With this theory, one can also explore how the surface energy changes from the anhydrous state to the fully hydrated state. The surface energy data decay rapidly at the initial coverages and eventually approach the bulk water surface energy of 0.072 J·m^{-2} at exceedingly large coverages, as plotted in Figures 6A and 7A. Interestingly, when the surface energies are plotted as a function of relative pressure instead, there seems to be a plateau in the data from 0.1 to 0.6, and also indicates a smaller increase in surface energy. This seems to contradict previous results^{19,45} that suggest the bulk water surface energy is achieved between relative pressures of 0.3–0.5. For example, Castro and Quach¹⁹

stated that the surface energy of γ -alumina reached the bulk water value at only $34 \text{ H}_2\text{O}\cdot\text{nm}^{-2}$. However, using an estimate⁴⁶ for the cross-sectional area of a water molecule as 0.1 nm^2 , one can show that this condition amounts to only three monolayers of coverage, which is unlikely to be thick enough to establish the bulk water phase from a thermodynamic standpoint. In addition, they¹⁹ have performed many more water adsorption experiments on hydrated powders (starting at relative pressures of 0.3–0.5) and found that all of the specimens had an initial surface energy different from that of the liquid water. Here we show that surface energy data only begins to drop between a relative pressure of 0.6–0.7, which corresponds to 10–100 monolayers of thickness, a more physically reasonable condition considering the thermodynamics of the system. The observed behavior is somehow similar to those calculated by Digne et al.⁴⁵ using DFT of individual planes of γ -alumina. That is, as water coverage increases, the associated changes in the surface energy decrease, such that much of the changes occur within the first monolayers. The difference as compared to Castro and Quach's work¹⁹ can be attributed to the role of nonadsorbed water chemical potentials (neglected in their work). Note that this will affect the water covered surface energies but not the anhydrous surface energy. That is, Castro and Quach proposed the usage of a single equation with heats summed up over the adsorption process from the liquid-like to the anhydrous state. The first point where the liquid-like behavior is seen is supposed to be used in the calculations. This diminishes the impact of the water molecules chemical potentials that increases with coverage but do not allow a correct estimation of hydrated states of the surface. This simplification is acceptable when only anhydrous energies are of interest.

Another important aspect of the theory presented here is that it accurately predicts the kinetic effects of adsorption on the surface energy of the sample during the adsorption process. This is observed from the results for the different adsorption paths shown for the 10YSZ runs 1 and 2 (Figure 7a). Note the lower surface energy at a given adsorbed amount for the faster process (where water molecules do not have kinetics for optimal adsorption and, therefore, higher compensation of the surface energy). The fact that both converge to similar surface energies (within the error) at the anhydrous state and similar surface energies for very high coverages (not shown) support the Gibbs free energy physical constraint that all variables are state variables, which are path independent, where the surface energy is a variable in the Gibbs free energy.

Our model also allows the chemical potentials of the adsorbed water to be calculated using the Gibbs isotherm (eq 8) with the already collected surface energy data, which is not commonly commuted data from the other techniques.^{10,12,17–19} The chemical potential data for the adsorbed molecules are shown in Figures 6C and 7B as a function of water coverage in log space. The chemical potentials are extremely negative at the low coverages and increase rapidly to zero at large values. This conforms to the physical constraint that the liquid water's chemical potential is in equilibrium with the vapor phase at the outermost layer, being zero at saturation. These figures strike a similar resemblance to Santiago Castrillon's⁴⁷ (Figure 2 of their paper) theoretical simulations using molecular dynamics, where they plot an interaction energy between the surface and the water molecules, which compares well with the proposed data through the first law of thermodynamics. They show that the

water interactions with the particle's surface decay rapidly as the water layers increase in accordance with our calculated data.

CONCLUSIONS

Here we presented a novel water adsorption microcalorimetry model to describe both physically and mathematically the adsorption process. The model incorporates a comprehensive physical description which correctly predicts the paradoxes that have been seen with other theories and accurately calculates important surfaces energy data needed for future experiments and theoretical calculations. The model included the derivation of the thermodynamically relevant equations during the adsorption process and coupled with the Gibbs adsorption isotherm for two interfaces. The equations were combined to isolate the surface energy and chemical potentials as functions of water coverage, leading to the development of a second order differential equation for the surface energy of the specimen (eqs 18 and 19). These equations were then solved numerically using a custom written MATLAB 2010a after feeding with fitted experimental data from both water adsorption quantity and associated heat of adsorption. We have tested this method using two technologically relevant nanoparticles, yttria-doped zirconia (10YSZ) and γ -alumina, where the calculated surface energies for 10YSZ and γ -alumina are thus 1.54 ± 0.08 and $1.57 \pm 0.04 \text{ J}\cdot\text{m}^{-2}$.

The surface energy data decayed from the anhydrous condition to the bulk water surface energy at exceedingly large water coverages. However, when the data was plotted as a function of pressure there was a plateau and bump in the data which was unexpected when comparing to previous research. It was shown that the plateau made physical sense due to the thickness of the water required to establish a bulk water phase. Also, this model was able to correctly predict the path independence of the surface energies for the same powder under a different kinetic pathway. In addition, this technique allows one to calculate the chemical potentials of water during the adsorption process. Data which that correlated strongly with theoretical molecular dynamics simulations reported elsewhere.

APPENDIX

For a three-phase system with bulk phases α , β , and ϵ in equilibrium with two interfaces I_1 and I_2 , the total Gibbs free energy is given below, where U is the internal energy, V is the volume, P is the pressure, T is the absolute temperature, S is the entropy, μ_i is the chemical potential of the i -th constituent of each phase, and θ_i is the adsorbed amount of i -th constituent. The Gibbs free energy can be represented by a linear combination of all of the phases where we have explicitly factored out the surface excess term, where γ is the surface energy and SA is the surface area.

$$G = U + PV - TS + \sum_i \theta_i \mu_i \quad (\text{A.1})$$

$$G_T = G^\alpha + G^\beta + G^\epsilon + G^{I_1} + G^{I_2} + \gamma SA \quad (\text{A.2})$$

One can now take the derivative of eq A.2 and incorporate the Euler Theorem for homogeneous functions to express the differential Gibbs free energy in eq A.3

$$dG = \sum_{\alpha, \beta, \varepsilon, I_1, I_2} (dU + PdV + Vdp - TdS - SdT + \sum_i \theta_i d\mu_i + \sum_i d\theta_i \mu_i) + \gamma dSA + SAd\gamma \quad (\text{A.3})$$

Since this is a reversible process, one can utilize the first law of thermodynamics that states the change of the internal energy must equal the heat added, Q , plus the work done, W .

$$dU = \delta Q + \delta W \quad (\text{A.4})$$

Expanding the definition of eq A.4 with entropy and P – V work terms yield eq A.5, which can be substituted back into eq A.3, where W' is non P – V work.

$$(\delta Q + \delta W)_{\text{total}} = \sum_{\alpha, \beta, \varepsilon, I_1, I_2} (-PdV + TdS - \delta W') \quad (\text{A.5})$$

$$dG = \sum_{\alpha, \beta, \varepsilon, I_1, I_2} (Vdp - SdT + \sum_i \theta_i d\mu_i + \sum_i d\theta_i \mu_i) + SAd\gamma \quad (\text{A.6})$$

In eq A.6 it was implicitly assumed that the only non P – V work came from the creation of a new surface, γdSA . Next we will incorporate the Gibbs–Duhem equation for each phase, eq A.7, in order to reduce the number of variables in the equation.

$$dG = \sum_{\alpha, \beta, \varepsilon, I_1, I_2} (VdP - SdT + \sum_i \mu_i d\theta_i) \quad (\text{A.7})$$

Therefore, the terms not in eq A.7 must be equal to zero. Therefore, this new equation relates the change in the chemical potentials of the bulk phases and the interfaces to changes in the surface energy.

$$0 = \sum_{\alpha, \beta, \varepsilon, I_1, I_2} (\sum_i \theta_i d\mu_i) + SAd\gamma \quad (\text{A.8})$$

At equilibrium under constant temperature and pressure, the bulk phases have another condition from the Gibbs–Duhem equation that one can enforce, which is that the change in the chemical potentials must be negligible as well.

$$SAd\gamma = - \sum_{I_1, I_2} (\sum_i \theta_i d\mu_i) \quad (\text{A.9})$$

Therefore, eq A.9 is the general Gibbs adsorption isotherm for two interfaces, which consists of the adsorbent excess of the constituents in the interfaces and not in the bulk phases. This equation compares well with the single interface Gibbs adsorption isotherm, noting that the number of species summations is directly linked to the number of interfaces in the system and can be extended as such.

■ ASSOCIATED CONTENT

■ Supporting Information

Matlab code for surface energy calculation using the described method is available. This material is available free of charge via the Internet at <http://pubs.acs.org>.

■ AUTHOR INFORMATION

Corresponding Author

*E-mail: rhrcastro@ucdavis.edu. Fax: (530) 752-9307. Phone: (530) 752-3724.

Notes

The authors declare no competing financial interest.

■ ACKNOWLEDGMENTS

The author would like to thank NSF DMR CAREER 1055504 for financing the development of this method. J.W.D. was supported by the US Department of Energy, Office of Basic Energy Sciences. Dr. Dat Quach is acknowledged for the experimental results provided.

■ REFERENCES

- (1) Hammer, B.; Nørskov, J. K. Theoretical Surface Science and Catalysis—Calculations and Concepts. *Adv. Catal.* **2000**, *45*, 71–129.
- (2) Henry, C. R. Surface Studies of Supported Model Catalysts. *Surf. Sci. Rep.* **1998**, *31*, 231–325.
- (3) Han, X.; Jin, M.; Xie, S.; Kuang, Q.; Jiang, Z.; Jiang, Y.; Xie, Z.; Zheng, L. Synthesis of Tin Dioxide Octahedral Nanoparticles with Exposed High-Energy {221} Facets and Enhanced Gas-Sensing Properties. *Angew. Chem., Int. Ed.* **2009**, *48*, 9180–9183.
- (4) Zhou, Z.-Y.; Tian, N.; Li, J.-T.; Broadwell, I.; Sun, S.-G. Nanomaterials of High Surface Energy with Exceptional Properties in Catalysis and Energy Storage. *Chem. Soc. Rev.* **2011**, *40*, 4167–4185.
- (5) Liu, C.; Li, F.; Ma, L.-P.; Cheng, H.-M. Advanced Materials for Energy Storage. *Adv. Mater.* **2010**, *22*, E28–E62.
- (6) Linsebigler, A. L.; Lu, G.; Yates, J. T. Photocatalysis on TiO₂ Surfaces: Principles, Mechanisms, and Selected Results. *Chem. Rev.* **1995**, *95*, 735–758.
- (7) Jung, H. S.; Lee, J.-K.; Nastasi, M.; Lee, S.-W.; Kim, J.-Y.; Park, J.-S.; Hong, K. S.; Shin, H. Preparation of Nanoporous MgO-Coated TiO₂ Nanoparticles and Their Application to the Electrode of Dye-Sensitized Solar Cells. *Langmuir* **2005**, *21*, 10332–10335.
- (8) Vlachopoulos, N.; Liska, P.; Augustynski, J.; Grätzel, M. Very Efficient Visible Light Energy Harvesting and Conversion by Spectral Sensitization of High Surface Area Polycrystalline Titanium Dioxide Films. *J. Am. Chem. Soc.* **1988**, *110*, 1216–1220.
- (9) Castro, R. H. R.; Marcos, P. J. B.; Lorriaux, A.; Steil, M. C.; Gengembre, L.; Roussel, P.; Gouvea, D. Interface Excess and Polymorphic Stability of Nanosized Zirconia-Magnesia. *Chem. Mater.* **2008**, *20*, 3505–3511.
- (10) Castro, R. H. R.; Ushakov, S. V.; Gengembre, L.; Gouvea, D.; Navrotsky, A. Surface Energy and Thermodynamic Stability of γ -Alumina: Effect of Dopants and Water. *Chem. Mater.* **2006**, *18*, 1867–1872.
- (11) Navrotsky, A. Energetics of Oxide Nanoparticles. *Int. J. Quantum Chem.* **2009**, *109*, 2647–2657.
- (12) McHale, J. M.; Auroux, A.; Perrotta, A. J.; Navrotsky, A. Surface Energies and Thermodynamic Phase Stability in Nanocrystalline Aluminas. *Science* **1997**, *277*, 788–791.
- (13) Garvie, R. C. The Occurrence of Metastable Tetragonal Zirconia as a Crystallite Size Effect. *J. Phys. Chem.* **1965**, *69*, 1238–1243.
- (14) Garvie, R. C.; Nicholson, P. S. Phase Analysis in Zirconia Systems. *J. Am. Ceram. Soc.* **1972**, *55*, 303–305.
- (15) Triantafyllou, G.; Angelopoulos, G. N.; Nikolopoulos, P. Surface and Grain-Boundary Energies as Well as Surface Mass Transport in Polycrystalline Yttrium Oxide. *J. Mater. Sci.* **2010**, *45*, 2015–2022.
- (16) Kendall, K.; Alford, N. M.; Birchall, J. D. A New Method for Measuring the Surface-Energy of Solids. *Nature* **1987**, *325*, 794–796.
- (17) Ushakov, S. V.; Navrotsky, A. Direct Measurements of Water Adsorption Enthalpy on Hafnia and Zirconia Surfaces Using Novel Design for Gas Adsorption Microcalorimetry. *Appl. Phys. Lett.* **2005**, *87*, No. 164103–1–164103–4.
- (18) Zhang, P.; Xu, F.; Navrotsky, A.; Lee, J. S.; Kim, S.; Liu, J. Surface Enthalpies of Nanophase ZnO with Different Morphologies. *Chem. Mater.* **2007**, *19*, 5687–5693.
- (19) Castro, R. H. R.; Quach, D. V. Analysis of Anhydrous and Hydrated Surface Energies of γ -Al₂O₃ by Water Adsorption Microcalorimetry. *J. Phys. Chem. C* **2012**, *116*, 24726–24733.
- (20) Odelius, M. Mixed Molecular and Dissociative Water Adsorption on MgO[100]. *Phys. Rev. Lett.* **1999**, *82*, 3919–3922.
- (21) Schaub, R.; Thosttrup, P.; Lopez, N.; Lægsgaard, E.; Stensgaard, I.; Nørskov, J. K.; Besenbacher, F. Oxygen Vacancies as Active Sites for

Water Dissociation on Rutile $\text{TiO}_2(110)$. *Phys. Rev. Lett.* **2001**, *87*, 266104–1–266104–4.

(22) Henderson, M. A. An HREELS and TPD Study of Water on $\text{TiO}_2(110)$: The Extent of Molecular Versus Dissociative Adsorption. *Surf. Sci.* **1996**, *355*, 151–166.

(23) Lindan, P. J.; Harrison, N.; Gillan, M. Mixed Dissociative and Molecular Adsorption of Water on the Rutile(110) Surface. *Phys. Rev. Lett.* **1998**, *80*, 762–765.

(24) Adamson, A. W. An Adsorption Model for Contact Angle and Spreading. *J. Colloid Interface Sci.* **1968**, *27*, 180–187.

(25) Schlangen, L. J. M.; Koopal, L. K.; Stuart, M. A. C.; Lyklema, J. Wettability–Thermodynamic Relationships between Vapor Adsorption and Wetting. *Colloids Surf., A* **1994**, *89*, 157–167.

(26) Brunauer, S.; Emmett, P. H.; Teller, E. Adsorption of Gases in Multimolecular Layers. *J. Am. Chem. Soc.* **1938**, *60*, 309–319.

(27) Churaev, N. V.; Setzer, M. J.; Adolphs, J. Influence of Surface Wettability on Adsorption Isotherms of Water Vapor. *J. Colloid Interface Sci.* **1998**, *197*, 327–333.

(28) Badmann, R.; Stockhausen, N.; Setzer, M. J. The Statistical Thickness and the Chemical Potential of Adsorbed Water Films. *J. Colloid Interface Sci.* **1981**, *82*, 534–542.

(29) Hill, T. L. Statistical Mechanics of Multimolecular Adsorption. I. *J. Chem. Phys.* **1946**, *14*, 263–267.

(30) Hill, T. L. Statistical Mechanics of Multimolecular Adsorption II. Localized and Mobile Adsorption and Absorption. *J. Chem. Phys.* **1946**, *14*, 441–453.

(31) Motomura, K.; Aratono, M.; Matubayasi, N.; Matuura, R. Thermodynamic Studies on Adsorption at Interfaces: III. Sodium Dodecyl Sulfate at Water/Hexane Interface. *J. Colloid Interface Sci.* **1978**, *67*, 247–254.

(32) Halsey, G. Physical Adsorption on Non-Uniform Surfaces. *J. Chem. Phys.* **1948**, *16*, 931–937.

(33) Theimer, O. On Multilayer Adsorption Isotherms. *Trans. Faraday Soc.* **1952**, *48*, 326–331.

(34) Vu, D.-H.; Wang, K.-S.; Chen, J.-H.; Nam, B. X.; Bac, B. H. A New Model for Water Adsorption in Porous Ceramics. *J. Porous Mater.* **2013**, *20*, 129–136.

(35) Yashima, M.; Ohtake, K.; Kakihana, M.; Yoshimura, M. Zirconia-13 Mol % Calcia Solid Solution Synthesis by the Polymerized Complex and Coprecipitation Routes. *J. Mater. Sci. Lett.* **1994**, *13*, 1564–1566.

(36) Yashima, M.; Kakihana, M.; Ishii, K.; Ikuma, Y.; Yoshimura, M. Synthesis of Metastable Tetragonal(T') Zirconia-Calcia Solid Solution by Pyrolysis of Organic Precursors and Coprecipitation Route. *J. Mater. Res.* **1996**, *11*, 1410–1420.

(37) Lee, K. T.; Lidie, A. A.; Jeon, S. Y.; Hitz, G. T.; Song, S. J.; Wachsmann, E. D. Highly Functional Nano-Scale Stabilized Bismuth Oxides Via Reverse Strike Co-Precipitation for Solid Oxide Fuel Cells. *J. Mater. Chem. A* **2013**, *1*, 6199–6207.

(38) Ushakov, S. V.; Dalalo, N.; Navrotsky, A. Gas Adsorption Microcalorimetry: Probing Energetics of Oxide Surfaces. *Geochim. Cosmochim. Acta* **2005**, *69*, 485–485.

(39) Ma, Y.; Castro, R. H. R.; Zhou, W.; Navrotsky, A. Surface Enthalpy and Enthalpy of Water Adsorption of Nanocrystalline Tin Dioxide. *J. Mater. Res.* **2011**, *26*, 848.

(40) Navrotsky, A.; Ma, C.; Lilova, K.; Birkner, N. Nanophase Transition Metal Oxides Show Large Thermodynamically Driven Shifts in Oxidation-Reduction Equilibria. *Science* **2010**, *330*, 199–201.

(41) Mazeina, L.; Deore, S.; Navrotsky, A. Energetics of Bulk and Nano-Akaganeite, B-Feooh: Enthalpy of Formation, Surface Enthalpy, and Enthalpy of Water Adsorption. *Chem. Mater.* **2006**, *18*, 1830–1838.

(42) Digne, M.; Sautet, P.; Raybaud, P.; Euzen, P.; Toulhoat, H. Hydroxyl Groups on γ -Alumina Surfaces: A DFT Study. *J. Catal.* **2002**, *211*, 1–5.

(43) Bolis, V.; Fubini, B.; Marchese, L.; Martra, G.; Costa, D. Hydrophilic and Hydrophobic Sites on Dehydrated Crystalline and Amorphous Silicas. *J. Chem. Soc., Faraday Trans.* **1991**, *87*, 497–505.

(44) Costa, G. C. C.; Ushakov, S. V.; Castro, R. H. R.; Navrotsky, A.; Muccillo, R. Calorimetric Measurement of Surface and Interface Enthalpies of Yttria-Stabilized Zirconia (YSZ). *Chem. Mater.* **2010**, *22*, 2937–2945.

(45) Digne, M.; Sautet, P.; Raybaud, P.; Euzen, P.; Toulhoat, H. Use of DFT to Achieve a Rational Understanding of Acid–Basic Properties of γ -Alumina Surfaces. *J. Catal.* **2004**, *226*, 54–68.

(46) Livingston, H. K. The Cross-Sectional Areas of Molecules Adsorbed on Solid Surfaces. *J. Colloid Sci.* **1949**, *4*, 447–458.

(47) Romero-Vargas Castrillón, S.; Giovambattista, N.; Aksay, I. A.; Debenedetti, P. G. Structure and Energetics of Thin Film Water. *J. Phys. Chem. C* **2011**, *115*, 4624–4635.

(48) Pinto, H. P.; Nieminen, R. M.; Elliott, S. D. Ab Initio Study of γ - Al_2O_3 Surfaces. *Phys. Rev. B* **2004**, *70*, 125402–1–125402–11.

(49) Xia, X.; Oldman, R.; Catlow, R. Computational Modeling Study of Bulk and Surface of Yttria-Stabilized Cubic Zirconia. *Chem. Mater.* **2009**, *21*, 3576–3585.